Atmospheric Environment 274 (2022) 118976

Contents lists available at ScienceDirect

Atmospheric Environment

journal homepage: www.elsevier.com/locate/atmosenv

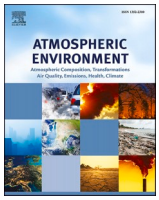

Circulation patterns influencing the concentration of pollutants in central Mexico

Yanet Díaz-Esteban [a], Bradford S. Barrett [b], Graciela B. Raga [a,*]

[a] Instituto de Ciencias de la Atmósfera y Cambio Climático, Universidad Nacional Autónoma de México, 04510, Ciudad de México, Mexico
[b] Air Force Office of Scientific Research, Arlington, VA, 22203, USA

HIGHLIGHTS

- Cluster analysis allowed the identification of pollution-related weather patterns.
- Dry-season high pollution in Mexico City is enhanced by mid-troposphere high pressures around 20°N.
- High pollution events are more frequent in March–May for O_3 and in December–February for NO_2 and $PM_{2.5}$
- La Niña (El Niño) favor the occurrence of patterns associated with more (less) pollution.

ARTICLE INFO

Keywords:
Circulation patterns
Air pollution
Synoptic climatology
Mexico City

ABSTRACT

In this study, weather patterns producing circulation features that result in poor air quality in the Mexico City basin during the dry season (November–May) were examined. Cluster analysis of the 500-hPa winds for a 30-year period (1990–2019) identifies a set of weather patterns that are then used to explore daily anomalous concentrations of ozone, nitrogen dioxide, and particulate matter. Above-normal levels of pollution occur under the influence of a mid-troposphere high pressure system centered around 20°N that shifts eastward over Mexico. This weather pattern is characterized by below-normal cloudiness, greater solar radiation, weaker surface winds, and a stronger morning temperature inversion that persists later than normal. High pollution events associated with this pattern occur preferentially during the dry season: March–May for O_3, and December–February for NO_2 and $PM_{2.5}$. PM_{10} events occurred evenly throughout the season. At the interannual scale, the El–Niño–Southern Oscillation is related to the frequency of pollution-related weather patterns: La–Niña (El–Niño) years favor the occurrence of patterns associated with more (less) pollution during the dry season. This work reveals the seasonality and predictability of pollution-related atmospheric patterns in the Mexico City basin, which can be used for air quality assessments at both seasonal and intraseasonal scales.

1. Introduction

The Mexico City Metropolitan Area (MCMA) is the most densely populated urban region in North America, with around 22 million inhabitants (Retama et al., 2015). Its geographic characteristics generally prevent ventilation of polluted air, as the city occupies a dried-up lake basin surrounded by locally higher topography. The area thus is highly prone to poor air quality, which often result in government-imposed environmental contingencies. Daily industrial, economic, and transport activities release gases and particulate matter that worsen air quality directly or act as precursors to secondary pollutants, such as ozone (O_3) and fine particles. Even though pollution levels have decreased since 1990 in Mexico City, Velasco and Retama (2017) reported that in recent years, 48–57% of days still exceed the World Health Organization (WHO) 8-h running average standard of 70 ppb for O_3. Additionally, annual mean values of particulate matter exceed both WHO and Mexican (NOM-025-SSA1-2014) standards (Fig. 1 of García-Franco (2020)). Outdoor air pollution is a major public health problem (Holgate, 2017; World Health Organization, 2018), associated with cardiovascular and respiratory diseases and cancers, among others, and especially in large megacities under changing climates (Baklanov et al., 2016). Thus, studies that seek to identify weather patterns that

* Corresponding author. Investigación Científica s/n, C.U., Coyoacán, 04510, Ciudad de México, Mexico.
E-mail addresses: yanet.diaz@atmosfera.unam.mx (Y. Díaz-Esteban), bradford.barrett@us.af.mil (B.S. Barrett), raga.graciela@gmail.com, raga@unam.mx (G.B. Raga).

https://doi.org/10.1016/j.atmosenv.2022.118976
Received 3 November 2021; Received in revised form 19 January 2022; Accepted 24 January 2022
Available online 9 February 2022

lead to unhealthy air pollution levels are useful.

Emissions are key to ambient pollution concentrations. However, local meteorological conditions also play an essential role in the occurrence of a poor air quality episode, as meteorology affects the formation, transport, and dispersion of pollutants (de Foy et al., 2006b; Bei et al., 2013). In turn, local meteorological conditions depend on synoptic-scale patterns that themselves vary at different timescales: interannual, seasonal, and intraseasonal. Fast and Zhong (1998); de Foy et al. (2005, 2008); Barrett and Raga (2016); Barrett et al. (2019); Silva-Quiroz et al. (2019) and García-Franco (2020) demonstrated that synoptic conditions significantly affect daily and seasonal evolution of pollutants by modulating local circulation, stability, and cloud cover. Other authors have highlighted the importance of smaller-scale meteorological forcing, including surface wind circulation, on the spatial distribution of air pollutants (Jauregui, 1988; Raga et al., 1999; Jazcilevich et al., 2005; de Foy et al., 2006a,b; Salcido et al., 2019). All of these studies focus on characterizing the behavior of air quality in Mexico City according to the type of synoptic and local-scale wind patterns. However, they tend to analyze only a few events, and none of them use neural network algorithms such as unsupervised clustering techniques that enable the analysis of hundreds of polluted events over the past several decades.

Clustering is an exploratory data analysis technique used to investigate the underlying structure in datasets. It groups observations based on their similar characteristics (Jain et al., 1999), and as such, it is suitable for discovering and extracting information that may have been previously unnoticed (Govender & Sivakumar, 2020). These type of unsupervised classification techniques can highlight significant features without user interference (Gonçalves et al., 2008). One of the most popular applications of cluster analysis in air pollution studies is the identification of synoptic conditions and their relationship with concentrations of pollutants (Govender & Sivakumar, 2020). This approach facilitates the organization and interpretation of large data volumes over long periods. The cluster analysis approach has been successfully applied in different regions of the world –such as the US, China and the United Kingdom– to understand the connection between large-scale atmospheric patterns and temporal and spatial variations in pollutants: Eder et al. (1994); McGregor and Bamzelis (1995); Comrie (1996); Chuang et al. (2008); Ngang and Byun (2011); Pearce et al. (2011); Hsu and Cheng (2016); Stauffer et al. (2016); Zhan et al. (2019); Hsu and Cheng (2019); Kotsakis et al. (2019).

This study employs a cluster analysis technique called Self-Organizing Maps to classify and analyze the synoptic-scale circulation patterns that have historically affected air pollution in the MCMA. Using this unsupervised algorithm, we aim to provide a clearer understanding of air quality-related atmospheric patterns that are recurrent during the dry season in Mexico. This work also analyzes the intraseasonal evolution of air pollution events, which has implications for subseasonal forecasts of dangerous air quality episodes. Additionally, the study explores the interannual variability of air quality through the connection between weather patterns and different climate modes.

2. Data and methods

2.1. Area and period of interest

The Mexico City Metropolitan Area is located in a basin at around 2300 m above sea level, surrounded by mountains up to more than 4500 m (Fig. 1 a). Fig. 1 b shows the annual average temperature and rainfall at the basin. The rainy or wet season spans from May to October. The rainfall amount peaks between June and September, with values much higher than at the beginning (May) or the end (October) of the season. For the rest of the year, low rainfall is observed at the basin. The mean temperature shows a marked annual cycle, with a maximum during April and May and a minimum from November to February.

High pollution events in the MCMA are most frequent during the dry season (Retama et al., 2015; Barrett and Raga, 2016; Silva-Quiroz et al., 2019). Then, this work focus on the months ranging from November to May –the time of the year with less rainfall–, for the period 1990–2019. The November–May season, from here on the "dry season", is further divided into two sub-seasons: the dry-cold (November to February) and the dry-warm (March to May), which are the most used classifications for air quality studies in central Mexico. During the dry-warm season the highest concentrations of pollutants occur in the MCMA, with environmental contingencies that force the local government to restrict vehicular circulation and other everyday activities.

2.2. Identification of the weather patterns

A cluster analysis is applied to determine which weather patterns (WPs) are related to the highest and lowest daily concentrations of pollutants in the Mexico City Metropolitan Area during a 30-year period. Cluster analysis allows the objective classification of several input variables, whose output is a set of groups that minimize variance within each group and maximize variance between them (Hsu and Cheng, 2019). Although several methods exists for cluster analysis, we employ a neural network technique called Self-Organizing Maps (SOM) (Kohonen, 1982, 2001), which has been widely applied in meteorology in the tropics and extratropics (Liu and Weisberg, 2011) as well as in synoptic climatology (Sheridan and Lee, 2011; Henderson et al., 2017; Díaz-Esteban and Raga, 2018). A detailed description of the SOM method can be found in many papers, such as in Vesanto and Alhoniemi (2000) and Elghazel and Benabdeslem (2014). The number of clusters (N), in this study representing the synoptic or weather patterns, is determined

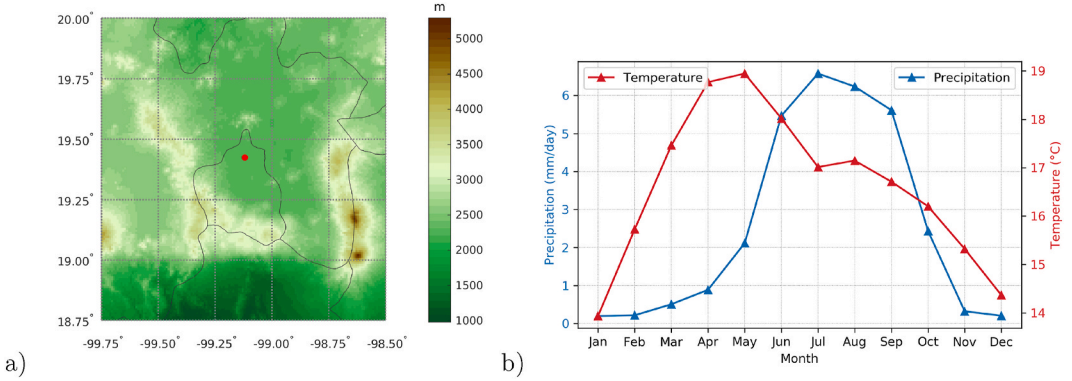

Fig. 1. a) Topography of the Mexico City Metropolitan Area with state boundaries in contours. The location of Merced station is indicated as a red dot. b) Mean annual cycle of precipitation and temperature for the period 1977–2016. (For interpretation of the references to colour in this figure legend, the reader is referred to the Web version of this article.)

by computing the Davies-Bouldin index (Davies and Bouldin, 1979), which is a measure of the quality of the clustering depending on the characteristics of the dataset. A lower value of the index will mean that the within-cluster scatter is lower than the cluster separation, therefore indicating a good clustering. As showed in Figure SM1 of Supplementary Material, the best choice is N = 7 clusters, so we selected a total of seven nodes for the analysis. Also, a review of the literature on this subject reveals that around five to seven clusters can be sufficient to describe the main atmospheric features related to air pollution in cities.

An area centered over central Mexico (12–32°N; 120–85°W) was selected for the cluster analysis. This area covers Mexico and its adjacent seas: the Gulf of Mexico, the Tropical Eastern Pacific, and a portion of the Caribbean Sea. The selection of that area allows to account for synoptic-scale systems that affect Mexico City on scales from a few hundred to several thousand kilometers.

Daily values are introduced to the SOM algorithm to obtain the patterns. Days from 1 November of a given year to 31 May of the next are taken, for a 30-year period, resulting in a total of 6367 daily values (212 days × 30 years, plus 29 February from seven leap years in the period 1990–2019). Some preprocessing is required to this daily values before applying the SOM algorithm. First, standardized anomalies are computed by subtracting the corresponding long-term mean to daily values and dividing by their standard deviation. For example, for 1 November 1990, the standardized anomaly is the value of that day minus the mean value for all 1 November on the study period, divided by the standard deviation of all 1 November. Additionally, anomalies are weighted by the cosine of latitude to account for the dependence of the grid-point density on latitude.

Once the cluster analysis is complete, the SOM algorithm generates a non-linear classification of the daily dataset and separates each day into seven categories or weather patterns. Then, composite anomaly maps of atmospheric variables are constructed to characterize the patterns.

2.3. Data

Data from several different sources are analyzed in this study. The government air quality network, Red Automática de Monitoreo Atmosférico (Automated Atmospheric Monitoring Network, RAMA), measures all criteria pollutants in MCMA since 1986 (although only a few stations have records dating back to 1986). We selected only one station from RAMA (Fig. 1 a) —which contains the longest and most complete record— because the behavior of pollutants for nearby stations under the same large-scale atmospheric circulation pattern does not differ significantly, as showed by Barrett et al. (2019) and in Supplementary Material (Figures SM2 to SM5). We obtain RAMA hourly measurements of a number of pollutants: O_3, NO_2, and particulate matter smaller that 2.5 μm($PM_{2.5}$) and 10 μm(PM_{10}). The RAMA dataset also provides hourly surface meteorological observations of temperature, relative humidity, surface pressure, wind speed, and wind direction. All variables (pollutants measurements and meteorological observations) are available for the entire study period (1990–2019), except for PM_{10} that covers 1995–2019, and $PM_{2.5}$ that are available for 2003–2019.

We also analyzed characteristics of the morning temperature inversion in the MCMA: the inversion thickness, the near-surface temperature required to overcome the inversion, and the time of the day when this occurs, in hours. The inversion thickness is measured as the difference, in meters, between the bottom and top layers that comprise the temperature inversion, and indicates its strength. A stronger inversion will require a warmer near-surface temperature to erode it, and it will take longer, thus delaying inversion erosion. Thus, these three metrics are indicative of the intensity of the morning temperature inversion. Daily values of these inversion metrics were obtained from the Dirección de Monitoreo de Calidad del Aire (Air Quality Monitoring Directorate) of Secretaría de Medio Ambiente (Environment Secretariat) of the Mexico City government. They estimate these metrics daily from the morning (12:00 UTC, 06:00 Local Time) radiosonde launch in the city.

Daily *u* and *v* wind components at 500 hPa from the ERA5 reanalysis (Hersbach et al., 2018) at 1°-horizontal resolution are the input to the clustering algorithm. Previous research has shown that the wind field can be useful to explain the behavior of high pollution events, since it can modulate the dispersion or the stagnation of pollutants. The 500-hPa pressure level was chosen to account for the circulation at a synoptic scale while excluding the influence of the topography of the study region. (Note that in central Mexico, the terrain height exceeds 5000 m in some locations; Fig. 1). The weather patterns were created using the 500-hPa circulation at 18:00 UTC (12:00 Local Time), but the results did not change when using the 500-hPa circulation at 12:00 UTC (06:00 Local Time) (not shown). Finally, for each weather pattern, we created daily composite maps of 500- and 700-hPa geopotential height, surface net shortwave radiation, surface temperature, total cloud cover, and wind at different heights, all from the ERA5 two-dimensional fields.

Composite diurnal cycles of hourly observations for each WP are also produced making use of the RAMA measurements. To obtain these composites, each day in the 1990–2019 period is classified into one of the seven WPs. Then daily time-series (24-h observations) of all days falling in the same category or WP are averaged. Finally, the long-term seasonal mean for the study period is subtracted from the daily mean values for each WP to obtain an anomaly.

Several climate indices that capture atmospheric and oceanic variability on the interannual timescale were used to examine their modulation of the synoptic patterns. Those indices are the Multivariate El–Niño–Southern Oscillation Index version 2 (MEIv2), the North Atlantic Oscillation (NAO), the Western Hemisphere Warm Pool (WHWP), and the Caribbean Warm Pool (CWP). WHWP and CWP indices are defined as the monthly anomaly of the area enclosed by the 28.5 °C sea surface temperature isotherm during the late summer in the Atlantic – Eastern North Pacific, and the Caribbean, respectively. The indices for MEIv2, NAO, and WHWP are obtained from https://psl.noaa.gov/data/climateindices/list/, and the CWP index is computed manually with data from OISSTv2 (Reynolds et al., 2002).

3. Results and discussion

3.1. Characterization of the weather patterns

The seven weather patterns reveal important circulation features on the synoptic scale. Each weather pattern is associated with a distinctive feature in geopotential height at 500 hPa. Table 1 summarizes for each WP the relative frequency, the total number of days, the two most common months, the mean persistence (before transitioning to another pattern), and the hourly average concentrations of O_3, NO_2, $PM_{2.5}$, and PM_{10}. Hourly averages of pollutants are obtained computing the mean value across all hourly measurements (0–23 h) for all days corresponding to the same WP.

WP1 is the most common pattern and the one with the longest persistence, while the other six have similar frequencies and duration. The frequencies of the patterns are unevenly distributed around the dry season, with WP1, WP3, WP4, and WP7 being more likely to occur during the dry-cold season and WP2, WP6, and WP5 during the dry-warm season, although in WP5 there is almost no difference in frequency between the two seasons (Fig. 2). Thus, there is evidence of intraseasonal variability in which pattern is favored during the dry season.

Fig. 3 shows composite maps of geopotential height and wind at 500 hPa for each WP. Similar composites for 700 hPa are shown in Figure SM6 of Supplementary Material. The clustering analysis revealed the dominant weather patterns in the study region for the dry season. WP1 features a mid-troposphere ridge centered in the Eastern Tropical Pacific (around 18°N and 108°W) with a closed anticyclonic circulation. It also shows large positive anomalies (80 m) in geopotential height over northern Mexico and southwestern US. WP2 and WP3 have similar ridge

Table 1
Relative frequency of occurrence, number of days, first and second month of highest occurrence and hourly mean O_3, NO_2, $PM_{2.5}$, and PM_{10} for each weather pattern.

Weather Pattern	Relative Frequency (%)	Number of days	1st/2 nd month of highest occurrence	Mean persistence (days)	Hourly mean concentration			
					O_3 (ppb)	NO_2 (ppm)	$PM_{2.5}$ ($\mu g/m^3$)	PM_{10} ($\mu g/m^3$)
WP1	17.9	1137	Dec/Mar	3.33	31.9	42.1	30.8	68.2
WP2	14.1	897	May/Apr	2.82	35.1	43.0	32.9	71.9
WP3	13.6	868	Feb/Dec	3.18	38.3	46.2	34.1	73.6
WP4	12.7	807	Nov/Dec	2.70	34.9	45.0	32.0	67.9
WP5	13.2	839	Apr/Jan	2.78	30.3	41.2	27.6	63.5
WP6	13.9	886	May/Apr	2.74	31.5	41.9	28.2	64.4
WP7	14.7	933	Mar/Jan	3.12	29.9	40.7	28.5	62.1

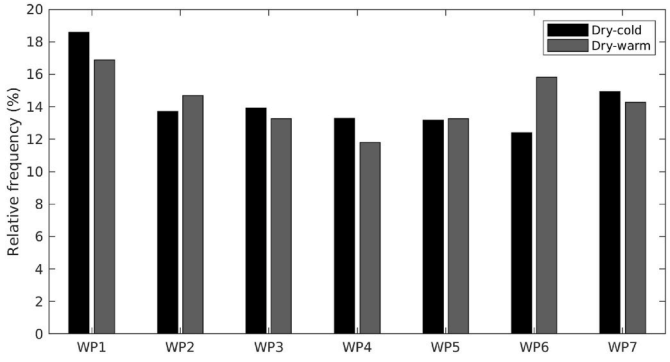

Fig. 2. Relative seasonal frequencies of each weather pattern. For each of the two seasons, the frequencies add up to 100%.

patterns located farther east; the center of the high pressure in WP2 is located over central Mexico, around 18°N and 100°W, while in WP3, it is located in the southern Gulf of Mexico around 18°N and 93°W. Moreover, a dipole pattern of geopotential height anomalies is evident in WP3 north of 23°N, with negative anomalies at northwestern Mexico and positive ones at eastern Mexico. WP4 presents a strong latitudinal pressure gradient, also evident in the wind pattern, with intense speeds near 20 m/s. Broad positive geopotential height anomalies are located equatorwards of 20°N in WP1, WP2, WP3, and WP4, but the largest anomalies are found farther north, closer to the subtropics. WP5 and WP6 exhibit negative geopotential height anomalies over all the region of interest, reaching −80 m in northern Mexico in WP5, associated with a mid-latitude trough affecting most of Mexico and adjacent seas, with strong winds and cold air advection from mid-latitudes to the tropics. These mid-latitude troughs at 500 hPa are related to extratropical cyclones and surface cold fronts affecting Mexico. The trough axis in WP5 extends over northwestern Mexico and the southwestern US; in WP6 the trough axis is located slightly to the east over north-eastern Mexico. WP7 also presents negative geopotential height anomalies over much of the area, with an incipient dipole pattern north of 20°N. The trough axis in WP7 extends from southern Texas and Louisiana to the Bay of Campeche in southern Mexico.

The synoptic patterns obtained are typical of wintertime in the study region, when the subtropical jet stream plays an important role in synoptic conditions, allowing mid-latitude waves –with their troughs and ridges– to transit from west to east over Mexico, the US, and Canada (Sheppard et al., 2002).

Anomaly composites of net surface shortwave radiation and 700-hPa temperature for the seven weather patterns identified in the SOM analysis are shown in Fig. 4. Above-average solar radiation is seen over central Mexico in WP1–WP4, with anomalies up to 50 W m^{-2}, consistent with positive 700-hPa temperature anomalies. Conversely, below-average radiation is observed during WP5–WP7 over most of Mexico, associated with below-average 700-hPa temperatures, with anomalies as low as −2 °C. In WP1 and WP5, both positive and negative temperature anomalies coexist over central Mexico. Notice that the broad band of positive radiation anomalies is located further southeast in WP4 than in WP3, WP2, and WP1. Likewise, the area with large negative anomalies is farther southeast in WP7 compared to WP6 and WP5. The geographic progression in features from one WP to the next is in line with typical eastward movement of those features during the dry season. This suggests a possible progression in the atmosphere from one WP to the next that would affect local weather as well as air quality in the MCMA.

More details of the local meteorological characteristics of the WPs in the study domain are provided by the composite diurnal cycles of

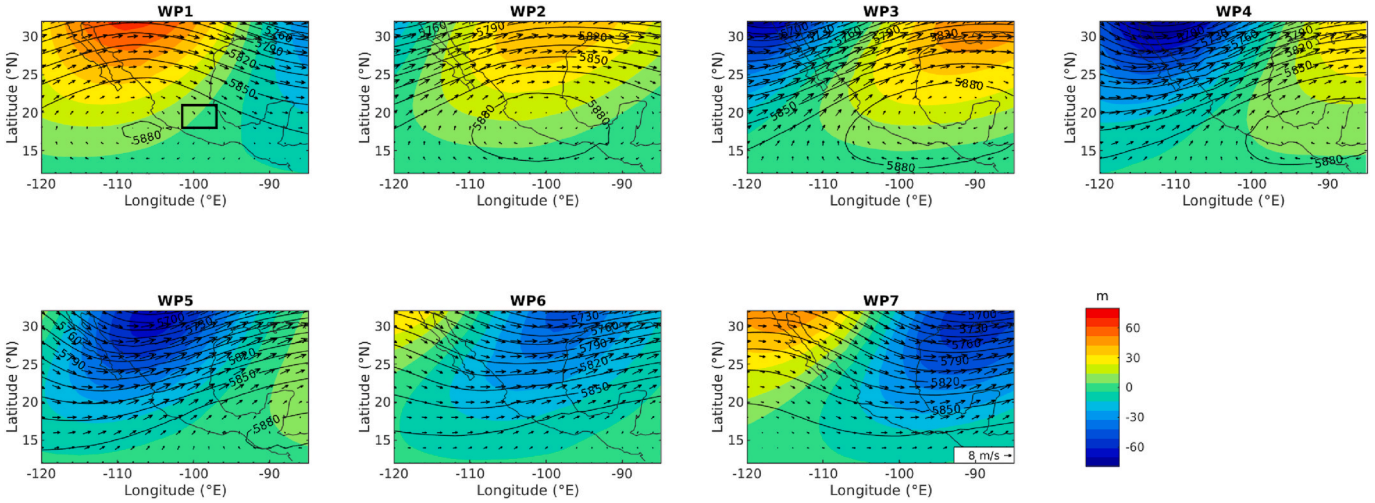

Fig. 3. Composites of mean 500-hPa geopotential height (contours, in m), their anomalies (shading, in m) and mean 500-hPa wind (vectors, in m/s), for each weather pattern. Box in WP1 defines the area where further and more detailed analysis is focused.

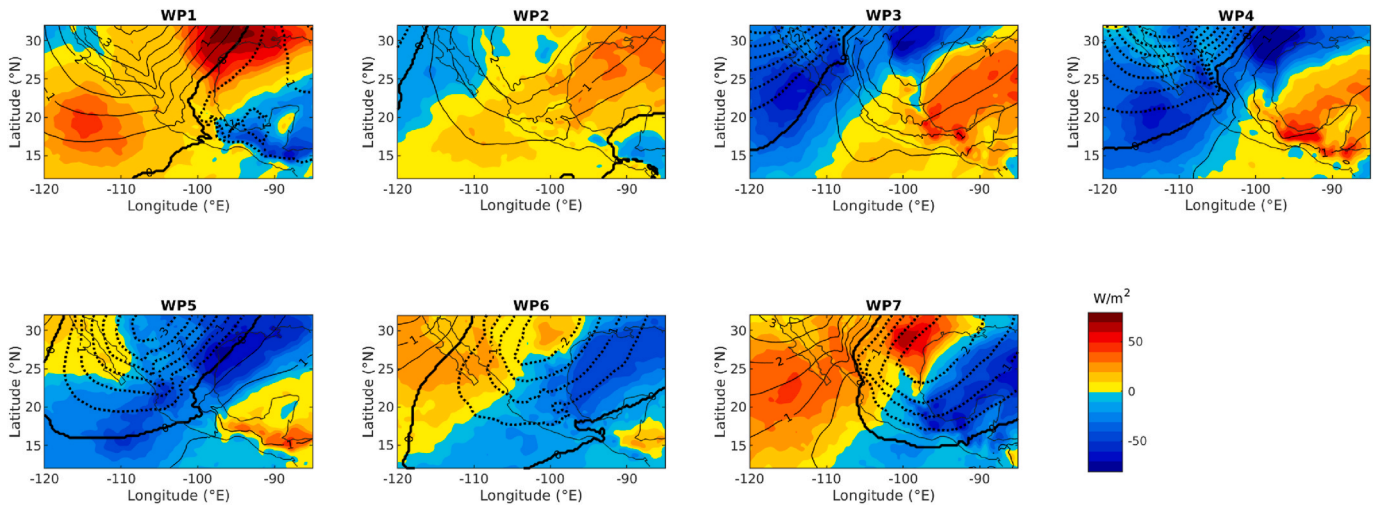

Fig. 4. Anomaly composites of surface net shortwave radiation (shading, in W m^{-2}) and near surface temperature (contours, in °C) for each weather pattern. Solid (dashed) contours indicate positive (negative) anomalies and the zero contour is highlighted in bold.

surface temperature, relative humidity, atmospheric pressure, and wind measured at the RAMA station (Fig. 5). The composites are presented in terms of anomalies, to highlight the relevant behavior of the WPs.

WP1 is the most frequent pattern identified by the clustering technique (occurring on 1137 days) and is also the most persistent (3.33 days long). Thus, when this pattern occurs, it is likely to remain for several days. WP1 is more frequent during the dry-cold season, particularly in December, although it also occurs in March during the dry-warm season. This WP is associated with anomalously cold temperatures and below-average relative humidity. Although temperatures rise during the course of the day, they are still colder than average (Fig. 5 a). WP1 also evidences above-average surface pressure, below-average wind speed, and northeasterly surface (10-m) winds. WP1 features a mid-troposphere ridge with a closed anticyclonic circulation in the eastern tropical Pacific, which is shifted eastward at 700 hPa and is, thus, located over central Mexico (Figure SM6 of Supplementary Material).

WP2 and WP3 behave similarly to each other, exhibiting anomalously warm and dry air, with a slight increase in atmospheric pressure and relatively weak surface wind speeds, particularly in WP3 (Fig. 5). Northeasterly flow prevails over the MCMA (negative *u* and *v*), as a result of a clockwise circulation around a mid-tropospheric high pressure system centered in central Mexico in WP2, a feature that is slightly displaced to the east over the Bay of Campeche in WP3 (Fig. 3). The high pressure system extends to the lower levels of the troposphere, and an anticyclone with a corresponding clockwise flow is also present at 700 hPa (Figure SM6 of Supplementary Material). Subsidence associated

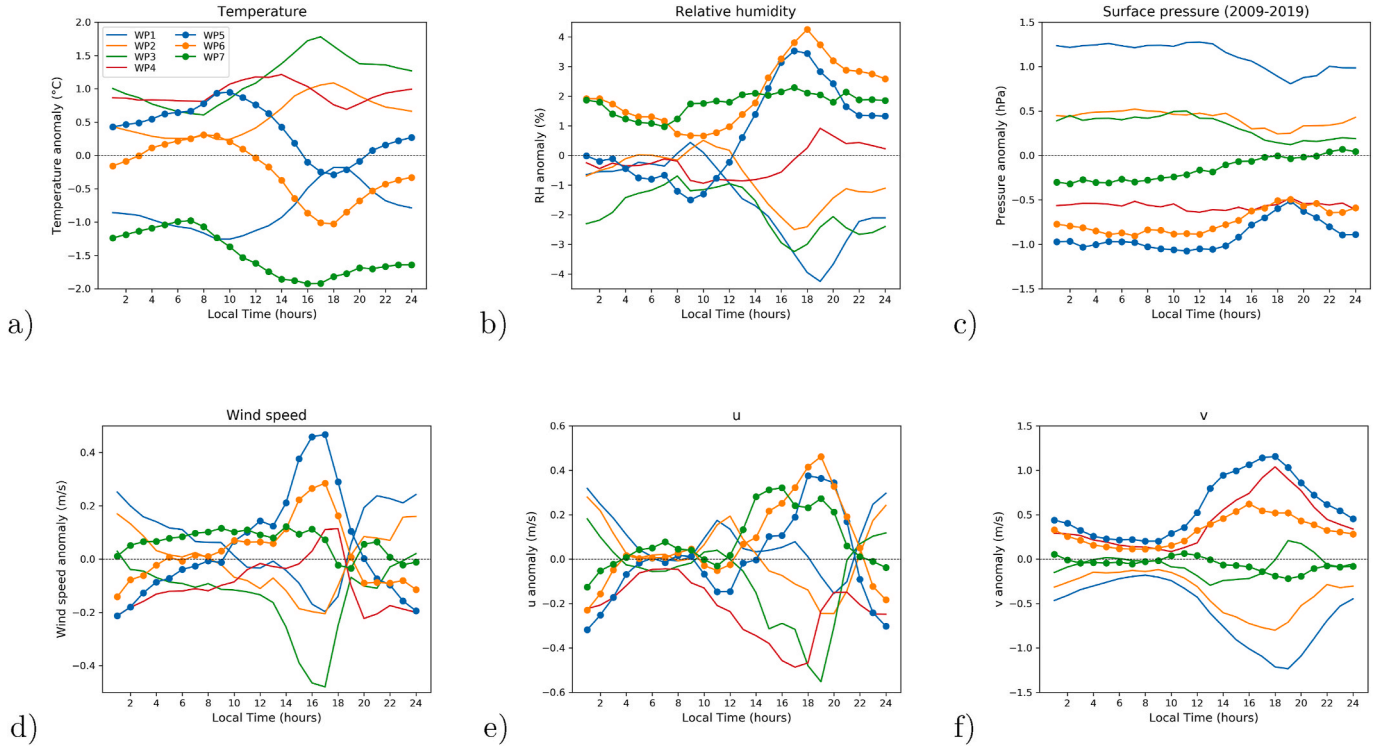

Fig. 5. Diurnal cycles of meteorological variables in the Mexico City Metropolitan Area, in terms of anomalies with respect to the long term seasonal average, for each weather pattern.

with these anticyclones suppresses convection, leading to increases in insolation and temperature, as observed in Fig. 4.

WP4 is more frequent during the dry-cold months, particularly in November, corresponding to the beginning of the dry season and possibly representing a transition from the wet to the dry season. This suggests that WP4 is associated with a weak and decreasing influence of the westward extension of the North Atlantic Subtropical High (NASH), which dominates over the Gulf of Mexico and the Caribbean in boreal summer (Romero-Centeno et al., 2007; Curtis and Gamble, 2008; Díaz-Esteban and Raga, 2018; Perdigón-Morales et al., 2018). In fact, in composite maps at 500 and 700 hPa (Fig. 3 and SM6, respectively), the weak NASH return circulation can be seen over the southeastern Gulf of Mexico, in conjunction with a more intense subtropical flow in the northwestern part of the domain. This highlights the coexistence of synoptic systems of two different seasons in this "transition" regime. The anomaly pattern of surface net solar radiation (Fig. 4) supports the coexistence of both the return circulation and the intense subtropical flow, with a very pronounced boundary between positive and negative anomalies located across central Mexico. As a consequence, there is no particularly distinctive behavior in the anomalies of relative humidity and surface wind speed in this WP (Fig. 5).

WP5–WP7 tend to behave similarly, with higher relative humidity, lower surface pressure, faster wind speeds, and more westerly (positive *u*) and southerly (positive *v*) winds (though the latter is less evident in WP7) (Fig. 5). This behavior indicates the influence of the mid-latitude trough around 25–30°N (Fig. 3), and thus in these WPs, the MCMA is affected by easterly to southwesterly mid-tropospheric flow. This flow is more evident in WP5 and WP6, where the trough axis is over western and northern-central Mexico, respectively, and less evident in WP7 because the trough axis is already positioned to the east, over southern Texas and northern Gulf of Mexico. This southward intrusion of the mid-latitude trough is also responsible for the increase in the pressure gradient at low levels, which explains the strong surface wind speed observed in those WPs, particularly in WP5 and WP6. The synoptic patterns observed in WP5–WP7 are associated with a decrease in atmospheric pressure, anomalous low temperatures, and an increase in humidity and wind speeds.

3.2. Diurnal cycle of air pollutants for the WPs

This section explores the relationship between air pollution and the synoptic patterns described above. Fig. 6 shows the diurnal cycle of anomalies of air pollutants under each WP, computed is the same way as those shown in Fig. 5. We expect that pollution anomalies would behave distinctly under different weather patterns, given the ability of the SOM algorithm to distinguish between atmospheric regimes. Indeed, pollutants evolve similarly, with negative anomalies under WP5–WP7 and positive anomalies under WP1–WP4.

Tropospheric ozone is a secondary pollutant produced by photochemical processes acting on anthropogenic emissions (Barrett and Raga, 2016). Thus, high values of both precursor gases and solar radiation are needed for ozone production. Maximum daily ozone (Fig. 6 a) is observed around 14:00 Local Time (LT) (Figure SM7 of the Supplementary Material). Anomalously high O_3 concentrations are associated with WP2 and WP3, with values up to 17 ppb for WP3, being the most extreme values in the period studied. Anomaly composites of total cloud

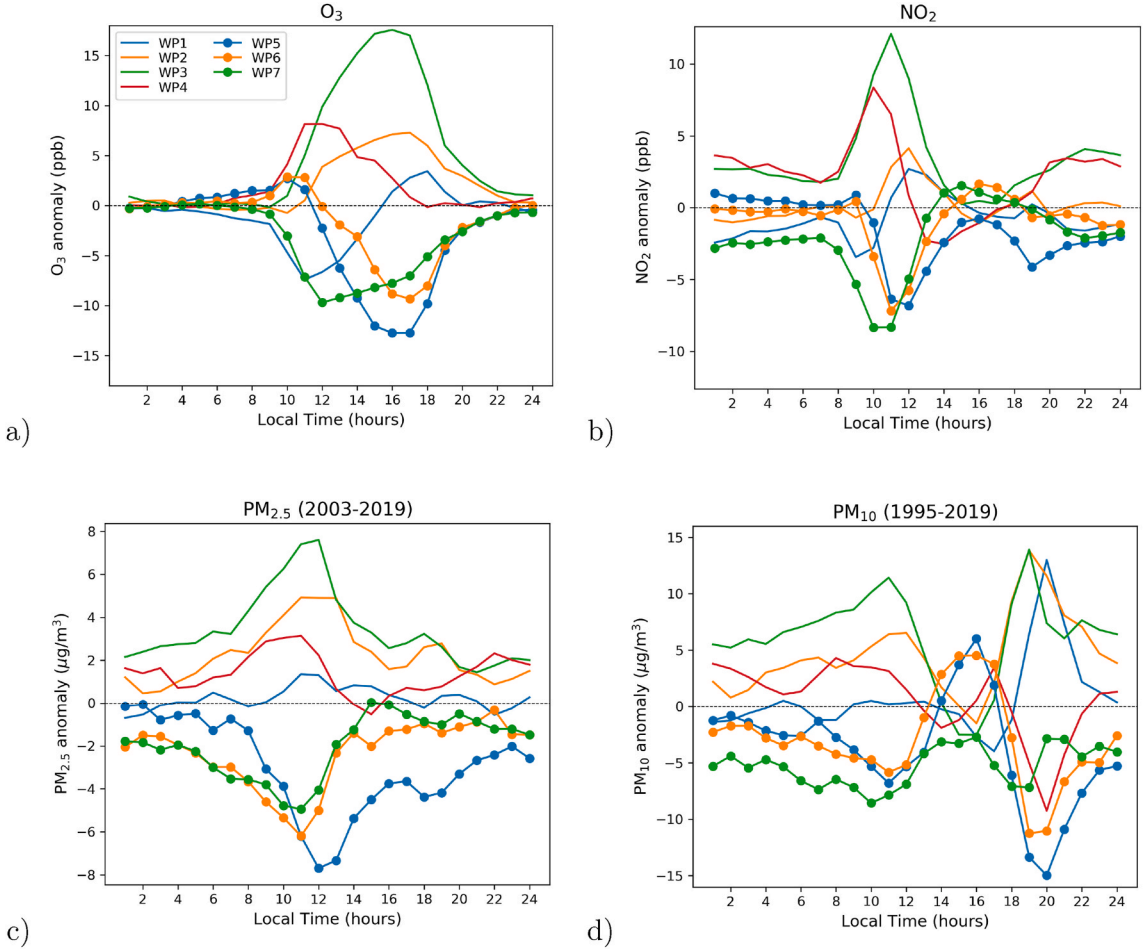

Fig. 6. Diurnal cycles of pollutants in the Mexico City Metropolitan Area, in terms of anomalies with respect to the long term seasonal average, for each weather pattern.

cover for the MCMA (Fig. 7) reveal that WP2 and WP3 have below-normal cloudiness —and thus, above-normal radiation— as a result of subsidence associated with high pressure centers inhibiting vertical motion. On the other hand, WP5, WP6, and WP7 feature negative O_3 anomalies, with the most negative values associated with WP5 (~ −14 ppb). These WPs result in more cloudiness over the MCMA (Fig. 7), as a result of the large-scale ascent associated with a synoptic-scale trough. Interestingly, WP4 is associated with above-normal O_3 concentrations despite having higher-than-average cloud cover (Fig. 7). Also, the anomalous O_3 peak in WP4 occurs earlier (~ 12:00 LT) when compared with the peaks in WP2 and WP3 (~ 16:00 LT), suggesting that the processes that are responsible for this anomaly differ from those in WP2 and WP3. One possible explanation for this O_3 peak at around 12:00 LT could be the accumulation of precursors and of O_3 itself during the previous night and early morning, due to a very strong residual layer and anomalously weak winds during the early morning, as shown in Fig. 5 d. This may induce the stagnation of O_3 and precursors, which can explain the maximum earlier in the day.

NO_2 is a primary anthropogenic pollutant and its major emission sources are combustion processes including power generation, heating, and engines in vehicles and ships (World Health Organization, 2018). Its diurnal maximum tends to occur between ~ 10:00 and 12:00 LT (Figure SM7 of the Supplementary Material), before the planetary boundary layer depth increases and turbulent circulations vertically disperse the emissions (Burgos-Cuevas et al., 2021). WP3 and WP4 show the largest NO_2 positive anomalies (Fig. 6 b) occurring between 10:00 and 11:00 LT, with values up to 12 ppb, while WP5, WP6, and WP7 are associated with negative anomalies (between 10:00 and 12:00 LT). Meteorological factors such as wind speed, wind direction, and subsidence, directly influence NO_2 ambient concentrations, and WP3 and WP4 have below-average wind speeds throughout the diurnal cycle, particularly WP3, which has the smallest negative anomalies. Composites of surface wind field (Fig. 8) show a west-east oriented surface confluence line in WP1 - WP4, particularly evident in WP3. The confluence line is seen in the central and northern part of Mexico City in WP3 and WP4, respectively, and is also observed in WP1 and WP2 but located further south. Confluence lines have been documented by Jazcilevich et al. (2005), de Foy et al. (2006a) and de Foy et al. (2008) as a mechanism for the accumulation of pollutants in Mexico City. As those authors showed, the maximum pollutant mixing ratios tend to follow confluence lines. Winds in WP5–WP7 are anomalously strong from 9:00 to 18:00 LT, and are transporting particles and gases away from the area, explaining the lower NO_2 values. Finally, WP1 and WP2 do not feature consistent diurnal cycles, with NO_2 anomalies ranging between −3 and 4 ppb, suggesting a small deviation from the mean diurnal values.

Particulate matter has a diversity of sources, including fossil fuels burning, natural sources, chemical reactions in the atmosphere. Thus, it tends to be a complex mixture of solid and liquid particles of organic and inorganic substances suspended in the air (World Health Organization, 2018). High concentrations of fine particulate matter result from a combination of primary and secondary contributions (Vega et al., 2002), and they can be impacted by factors such as wind velocity and direction, turbulent fluxes, mixing, and boundary layer height (Donateo et al., 2012; Liu et al., 2019). The diurnal cycle of the $PM_{2.5}$ (Fig. 6 c) show the opposite behavior of the polluted (WP1-WP4) and clean (WP5-WP7) circulation patterns. Since the diurnal peak in $PM_{2.5}$ occurs at ~ 11:00 LT (Figure SM7 of the Supplementary Material), it is expected that peak anomalies would occur around that time as well, with values between 5 and 8 $\mu g/m^3$ for WP2 and WP3 (Fig. 6 c). The polluted patterns (WP1–WP4) have nearly calm winds at the surface, indicating that mid-troposphere high-pressure regimes are more conducive to poor air quality, and particularly so when the mid-level high has a defined closed circulation located over south-central and south-eastern Mexico (WP2 and WP3, respectively). Anticyclones resembling these patterns tend to be associated with low wind speeds and well-defined surface confluence lines over southern and central Mexico City that act to concentrate the pollution in those parts of the city. In contrast, the clean WPs (WP5–WP7) have higher wind speeds with a more southerly component compared to other WPs (Fig. 5 d, f). This indicates that mid-latitude troughing can favor low values of $PM_{2.5}$ due to a decrease in atmospheric pressure, an increase in relative humidity, and advection of momentum, all of which enhance vertical mixing in the lower levels of the troposphere and favor both dispersion and the formation of clouds (Fig. 7).

The most polluted patterns for PM_{10} are also WP2 and WP3, presenting two daily maxima at ~ 11:00 and 19:00 LT with anomalies up to 14 $\mu g/m^3$ (Fig. 6 d). WP1 also features large positive anomalies of PM_{10}, up to 13 $\mu g/m^3$, but with only one daily peak at 20:00 LT. PM_{10} is (mostly) a primary pollutant emitted from anthropogenic activities, mainly vehicular traffic and fossil fuel burning (Lenschow et al., 2001; Salvador et al., 2004; Chow et al., 2002; Morton-Bermea et al., 2021), thus it has two peaks, coinciding approximately with the peak traffic hours (Figure SM7 of the Supplementary Material). The mechanisms that induce high concentrations of PM_{10} are similar to those of $PM_{2.5}$,

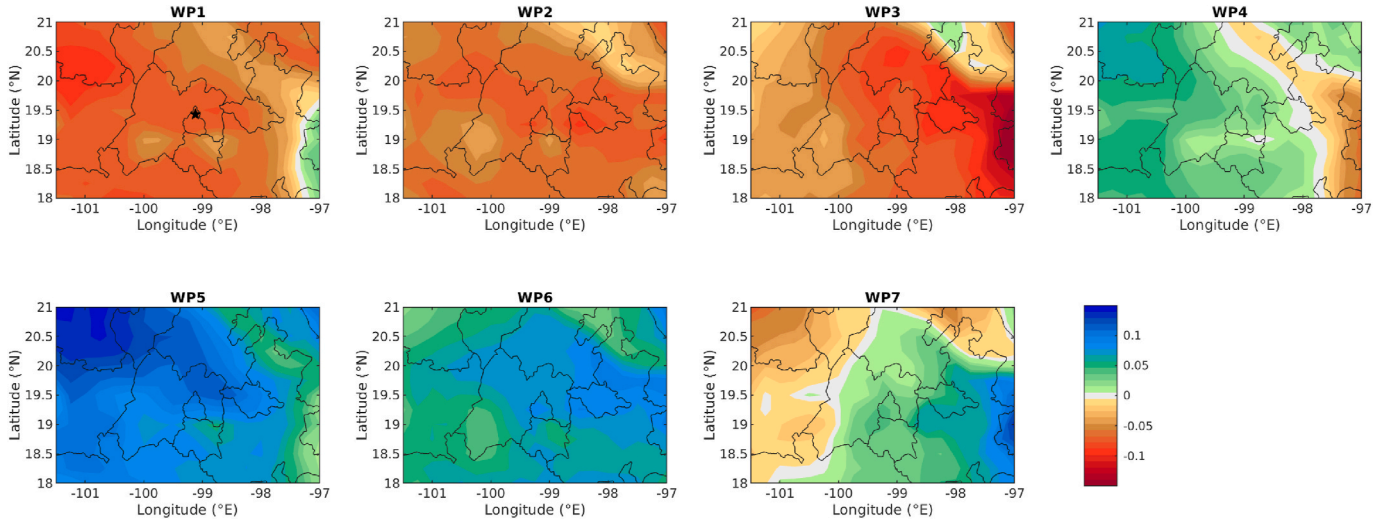

Fig. 7. Anomaly composites of total cloud cover over the MCMA, for each weather pattern. Black marker in WP1 indicates the location of Merced station.

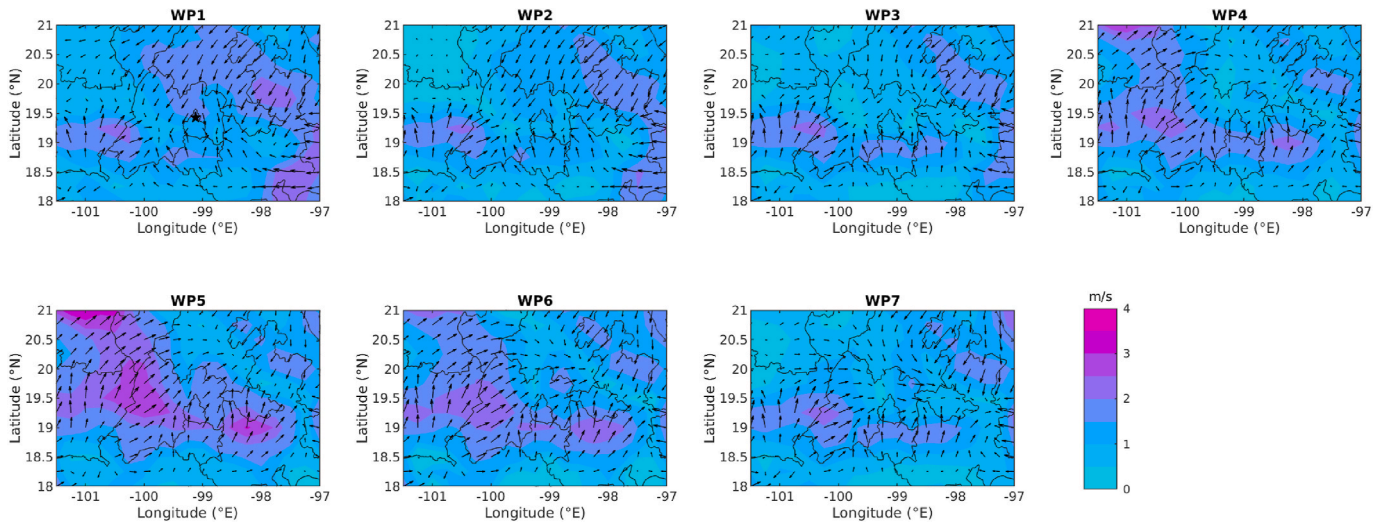

Fig. 8. Composites of mean 10-m wind (shading and vectors, in m/s) over the MCMA, for each weather pattern. Black marker in WP1 indicates the location of Merced station.

although with a lesser dependency on the accumulation of precursors and a larger reliance on immediate and local emissions. Two main causes can explain the high PM_{10} anomalies in those polluted WPs: first, low wind speeds that favor poor dispersion, and second, convergence along the well defined confluence line (Fig. 8) that favors pollutant accumulation along its axis. Mechanisms responsible for good air quality and low PM_{10} concentrations in WP5–WP7 are related to mid-latitude troughing, as explained for $PM_{2.5}$.

3.3. Impact of boundary layer processes on pollutants

Recent research has documented the importance of boundary layer processes in the concentration of pollutants and government-imposed environmental restrictions in Mexico City (Barrett et al., 2019; Pozo et al., 2019; Burgos-Cuevas et al., 2021). To characterize the boundary layer in the MCMA, we explore the boundary layer height (BLH) in the morning hours and the strength of the temperature inversion. In general, a stronger thermal inversion is a measure of a shallower boundary layer, which can increase the concentration of particles and gases near the surface. Also, Barrett et al. (2019) note that a deep boundary layer results in vertical mixing between contaminated near-surface air and unpolluted higher-layer air, causing a reduction of O_3 concentrations (when the air above the boundary layer is not itself polluted). The average BLH at 12:00 UTC (06:00 LT), the average thickness of the inversion, and the temperature at which the inversion erodes (T) for every weather pattern are plotted in Fig. 9.

During the early morning, the boundary layer over the MCMA is shallow due to the cool surface temperatures and radiational cooling during the night, especially in winter. It reaches a minimum height at roughly 07:00 LT. WP3 and WP4 exhibit the lowest values of BLH in the early morning (Fig. 9 a), leading to less mixing and more stagnant conditions during those weather patterns. For WP3, the temperature required to overcome the inversion is above 16 °C, which is the highest temperature among all the WPs (Fig. 9 b). WP3 also has the largest average inversion thickness (greater than 310 m), followed by WP2 and WP1. The thicker the thermal inversion, the harder it is for vertical parcel motions to extend beyond the boundary layer because more warming and turbulence is required near the surface. In fact, the inversion tends to be eroded later in WP3 (10:00 LT) when compared with the rest of the WPs (Fig. 10), which indicates that during WP3, the inversion lasts longer and polluted air remains trapped near the surface for longer hours. Note also that WP3 has the greatest frequencies for inversion erosion at hours as late as 12:00 and 13:00 LT (Fig. 10),

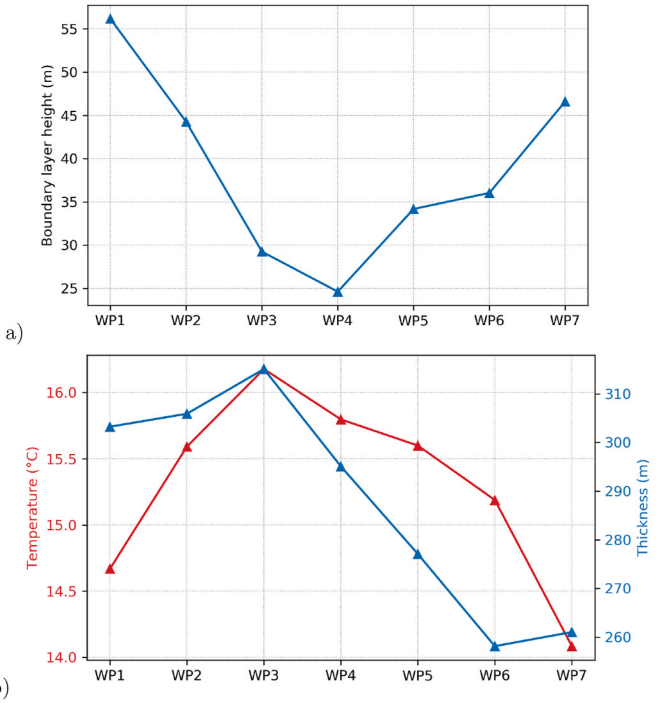

Fig. 9. a) Average boundary layer height and b) average inversion thickness and temperature at which the inversion erodes at the MCMA for each weather pattern.

indicating that when this pattern is present, the inversion will remain longer than in an average day.

In summary, the strong inversion and shallow boundary layer during the morning in WP3 favor the large accumulations of pollutants, resulting in the positive anomalies observed in Fig. 6, for both primarily and secondary pollutants (and note that WP3 shows the largest anomalies among all WPs in Fig. 6).

For the clean WPs (WP5–WP7), the inversion is weaker than average, particularly in WP6 and WP7 (Fig. 9 b), with a thickness of ~ 260 m and a T of ~ 14 °C (for WP7). This weaker inversion allows parcels to reach their lifting condensation levels quicker, promoting the development of clouds as the day goes by, as evidenced in Fig. 7. Probability densities of

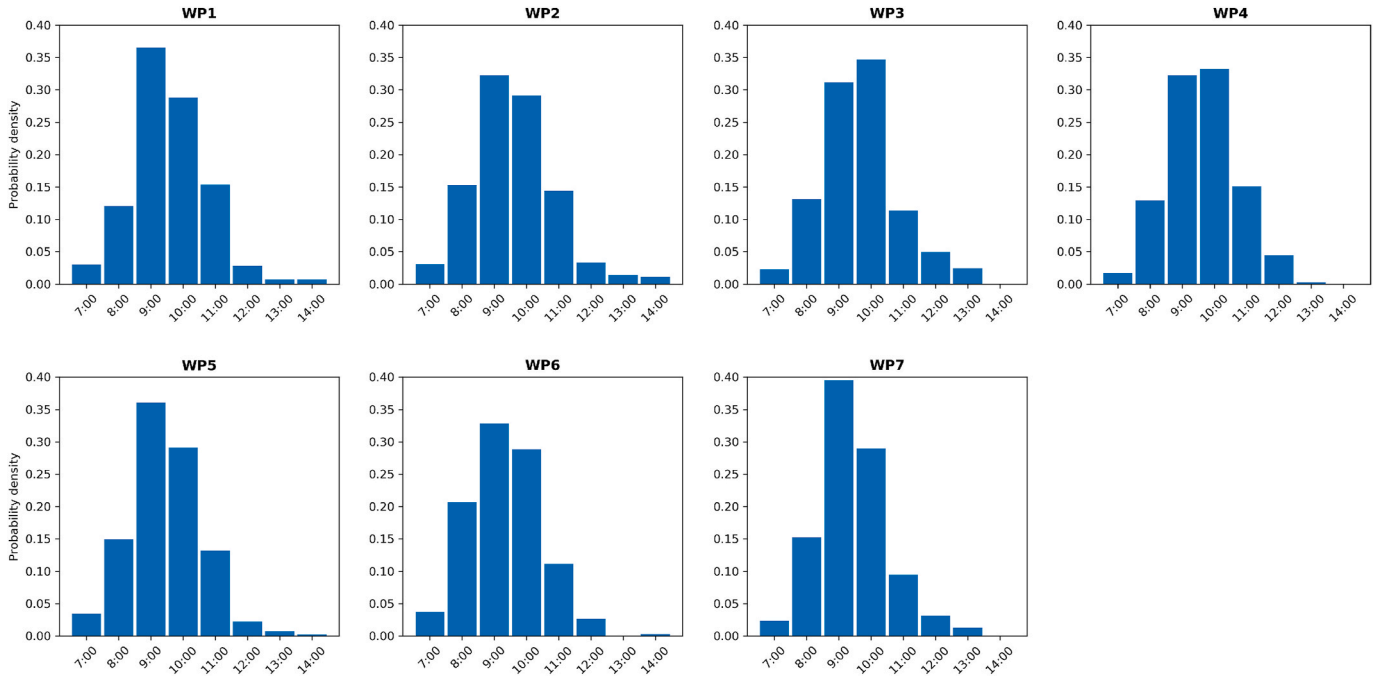

Fig. 10. Histograms for the hour at which temperature inversion erodes at the MCMA for each weather pattern.

the time when the temperature inversion erodes (Fig. 10) show that the most likely time to erode the temperature inversion during clean WPs is 09:00 LT. The early removal of the inversion enhances vertical mixing of clean air into the boundary layer and the dispersion of polluted air in the free atmosphere, a process that improve air quality during the day.

3.4. Intraseasonal and interannual variability of high pollution events

This section uses the derived weather patterns to explore air quality variability at intraseasonal and interannual timescales. A high pollution event (HPE) is defined as a day when the concentration of pollutants exceed the World Health Organization air quality guideline values (Table 2).

Fig. 11 shows the fraction of HPEs associated with each WP. To compute this quantity, we calculate the number of HPEs occurring under each WP and divide it by the total number of days in which each pattern occurs in the period 1990–2019. The fraction of HPEs is expressed as a percentage. The occurrence of HPEs varies as a function of pollutants and among regimes. Some weather patterns tend to produce more highly contaminated days than others, generally consistent across all pollutants. WP2–WP4 produce more HPEs within the study period, with WP3 being the most polluted pattern. In contrast, good air quality is associated with WP5–WP7, with WP5 being the cleanest for O_3 and $PM_{2.5}$, and WP7 the cleanest for PM_{10} and NO_2.

The seasonal evolution of HPEs for each WP is shown in Fig. 12. These graphics show two results: which WPs are associated with a larger number of HPEs, and the months in which those events are most frequent. This analysis provides insight of what to expect during the dry season and which patterns cause poor air quality, depending on the pollutant and time within the season. As expected from Fig. 11, WP3 is

Table 2
World Health Organization air quality guideline values.

Pollutant	Values	Averaging period
O_3	100 $\mu g/m^3$ (50 ppb)	8-h
NO_2	200 $\mu g/m^3$ (100 ppb)	1-h
$PM_{2.5}$	25 $\mu g/m^3$	24-h
PM_{10}	50 $\mu g/m^3$	24-h

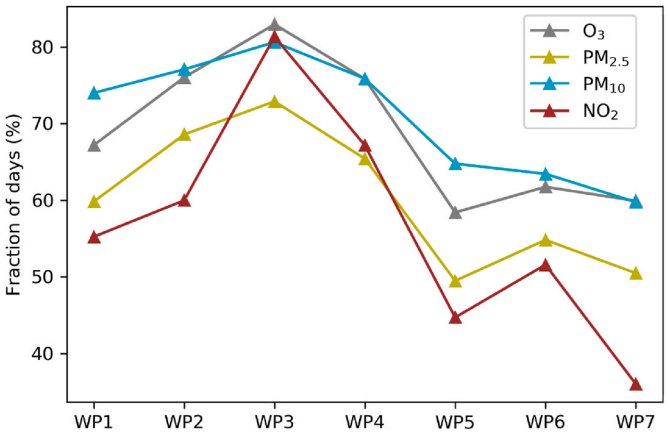

Fig. 11. Fraction of days where the concentration of pollutants exceeded the World Health Organization air quality guideline values, for each weather pattern.

the most polluted for all the contaminants. However, the number of HPEs varies throughout the season. For O_3 (Fig. 12 a), all WPs cause more events during March, April, and May, i.e. the dry-warm months, but WP2 and WP3 are associated with a larger number of events starting in February, where almost 90% of WP days are ozone HPEs. Conversely, for NO_2 (Fig. 12 b), most HPEs occur in December, January, and February, i.e. the dry-cold months, with the largest number of HPEs (between 35 and 45%) occurring with WP2 and WP3. During the dry-warm months, the WPs do not tend to be associated with HPEs for NO_2. This indicates that although WP2 and WP3 are the most polluted patterns, they produce even worse air quality for NO_2 during dry-cold months, i.e., at the beginning of the dry season. Similar behavior is seen for $PM_{2.5}$ (Fig. 12 c): WP2 and WP3 tend to produce more than 70% of the HPEs from December to February, while WP5–WP7 produce a small number of HPEs during all the season, particularly in February and March. For PM_{10} (Fig. 12 d), polluted weather patterns (WP1–WP4) tend to be associated with a large number of HPEs throughout all the dry season, and note that between 70 and 90% of days in those WPs are

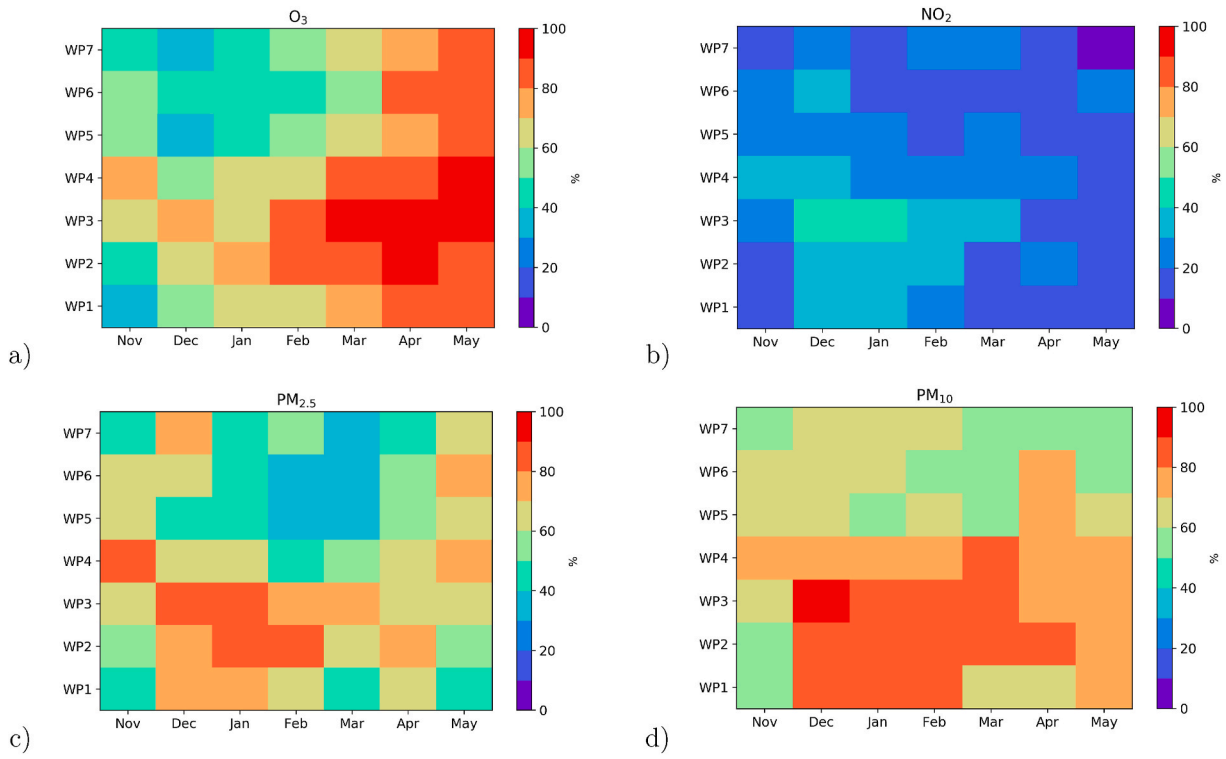

Fig. 12. Seasonal occurrence of high pollution events: fraction of polluted event days for every month and weather pattern.

HPEs. Therefore, the high concentrations of PM_{10} associated with WP1–WP4 are roughly equally distributed throughout the season.

The interannual variability of the synoptic patterns is examined through their relationship with low-frequency modes of variability that affect Mexico and adjacent areas on interannual timescales. Insight on such variability is important to evaluate potential skill in the predictability of the patterns and to anticipate possible government-imposed restrictions in the MCMA in response to bad air quality episodes. To explore this issue, we compute the seasonal frequencies of each synoptic pattern by adding up their monthly frequencies in a given season. For example, the frequency of a pattern in the 1990–1991 dry season is the sum of its frequencies in December and November of 1990 and its frequencies in January–May of 1991. The Pearson correlation coefficient between the WP-seasonal frequencies and several climate indices is then computed. This analysis was also performed considering separately the dry-cold season (November to February) and the dry-warm season (March to May), in order to evaluate whether the results for the entire dry season differ from those for any of the sub-seasons. Results are shown in Figure SM8 of Supplementary Material, and in general, no relevant differences are observed. The main details that follow apply to both the dry-warm and dry-cold seasons.

Fig. 13 shows the correlations between WP-seasonal frequencies and climate indices. Note the opposite behavior of the correlation curves of MEIv2 (blue) and CWP (green), which is not surprising because of the opposing remote influence of the El–Niño–Southern Oscillation (ENSO) and Caribbean sea surface temperatures on climate variability in southern and central Mexico (Díaz-Esteban and Raga, 2018; Rodríguez-Vera et al., 2019).

Polluted regimes (WP1–WP3) are negatively correlated with MEIv2, reaching a correlation coefficient up to −0.8 for WP1 (Fig. 13), indicating an increase in the frequency of those circulation patterns with a cold ENSO event, i.e. La–Niña (LN). Since values of November–December MEIv2 are used in this analysis, this result suggests that a mature phase of LN is associated with a larger occurrence of polluted regimes that cause more HPEs throughout the dry season. Previous work has found that LN events produce lower-than-average winter precipitation

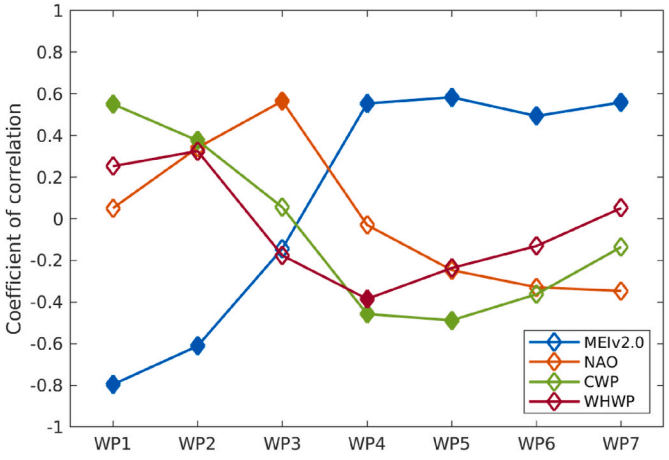

Fig. 13. Pearson product-moment correlation coefficient between various climate indices and the frequency of each WP, over the period 1990–2019. Filled markers indicate correlations significantly different from zero at the 95% level.

in northern and central Mexico (Magaña et al., 2003; Bravo-Cabrera et al., 2017; Bravo Cabrera et al., 2018). This supports our result that LN years favor a higher frequency of WPs that inhibit cloudiness and precipitation and cause poor air quality in the MCMA. Conversely, clean regimes (WP5–WP7) show significant positive correlations with MEIv2, suggesting that a mature warm ENSO or El–Niño (EN) event in November–December will favor the higher occurrence of clean regimes during the dry season, and therefore of less HPEs. During EN years, the mid-latitude jet stream interacts with a quasi-stationary Rossby wave known as Pacific-North American (PNA) pattern, causing a southward shift —and an increase in intensity— of the subtropical jet (Magaña and Quintanar, 1997). The anomalously intense jet stream is a track through which subtropical systems such as mid-latitude cyclones and cold fronts

can propagate southwards more frequently over northern Mexico (Magaña et al., 2003), causing an anomalously rainy and cold winter with greater ventilation in northern and central Mexico. This explains the positive relationship between EN events and WPs that are associated with good air quality in the MCMA.

The CWP index is computed for the late summer, particularly for the months of August–September preceding the dry season in a given year. They are chosen because the spatial extent of the CWP peaks in those months, and then gradually decreases. Fig. 13 shows the relationship with the seasonal frequencies of the WPs. WP1 and WP2 are positively correlated with the CWP index, i.e. an enhanced warm pool during the late summer is associated with increased frequencies of polluted patterns during the following boreal winter. As previously mentioned, a feedback mechanism between ENSO and the CWP is evident at interannual timescales. The intense anomalous convection in the tropical eastern Pacific during a developing warm ENSO event is connected with an enhanced subsidence in the Atlantic and the Caribbean, which leads to a further intensification of the surface trade winds and the Caribbean Low Level Jet. Therefore, during the development stage of an El Niño event –late summer and autumn– the sea surface temperatures in the Caribbean are anomalously cold. This supports our result that the WPs negatively correlated with MEIv2 in November–December are also positively correlated with the CWP index in the preceding summer months. The relationship between CWP and clean WPs is less robust, since only the correlations with WP5 are statistically significant at the 95% level (Fig. 13).

The NAO index only shows statistically significant relationship with the frequency of WP3 (Fig. 13), exhibiting a linear positive correlation of 0.56. Likewise, the WHWP index only has a significant negative correlation with the frequency of WP4 (−0.38). Thus there is no robust connection between either NAO or WHWP and the frequencies of WPs. However, it is notable that a similar tendency exists in the correlations between pollution and NAO, CWP, and WHWP, with all three having an inverse relationship with pollution compared to ENSO.

4. Conclusions

The relationship between large-scale atmospheric patterns prevalent during the dry season and severe pollution events in Mexico City was studied here. The analysis focused on some of the most dangerous pollutants for human health: ozone, NO_2, and particulate matter ($PM_{2.5}$ and PM_{10}). Higher-than-average concentrations of pollutants in the Mexico City basin occur under the influence of mid-troposphere high pressure centers. These anticyclones inhibit convection and cloud formation resulting in higher-than-average surface net solar radiation, negative anomalies in wind speed and relative humidity, positive anomalies in surface pressure and temperature, and feature a strong morning inversion that erodes later in the day. In contrast, lower-than-normal concentrations of pollutants are observed during weather patterns associated with an eastward-shifting mid-latitude trough over northern Mexico. Such troughs are associated with above-normal cloudiness and reduced net solar radiation, causing lower surface temperatures, an increase in relative humidity, and intense winds with southwesterly component.

The clustering technique employed in this paper –SOM– preserves the topology in the input data. This allows neurons to be combined on the basis of their similarity to each other; i.e., nearby clusters are more similar than distant ones. This represents a significant benefit for the interpretation of the underlying composite weather patterns, especially when analyzing transitions between them. By taking advantage of this feature, an evolution between the contiguous SOM patterns is detected through a transition matrix, which is useful to analyze the most likely sequence of regimes during the dry season, with possible implications for sub-seasonal forecast. The highly polluted WPs experience a sequence starting from WP1 to WP4, evidenced by the large probabilities of transition: WP1 $\xrightarrow{21.4\%}$ WP2 $\xrightarrow{26.2\%}$ WP3 $\xrightarrow{27.1\%}$ WP4 (Figure SM9 of Supplementary Material). That sequence involves an eastward displacement of a mid-level high around 20°N —starting from the eastern tropical Pacific, moving through central Mexico and reaching the southwestern Gulf of Mexico, driving the gradual increase of pollutants in a process that can last up to 10 days. Accordingly, the number of HPE increases from WP1 to WP3 in Fig. 11. Notice that although the sequence WP1 → WP2 → WP3 → WP4 has significantly large probabilities of transition, the backward sequence (WP4 → WP3 → WP2 → WP1) is not very likely, with probabilities under 15% (Figure SM9 of Supplementary Material). A large transition probability is also seen from WP7 to WP1 (25.2%), suggesting that a clean weather pattern with mid-latitude troughing, such as WP7, can be followed by high pressure systems over the eastern tropical Pacific (WP1), indicative of a transition towards a more polluted regime.

The analysis of intraseasonal variations in HPE as a function of the WPs showed that, although the seven WPs occur throughout the season, there is a preference for pollution events in certain parts of the season, and that preference varies depending on the pollutant (see Fig. 12). Polluted WPs tend to be associated with more O_3 HPEs during the dry-warm period (March to May). The polluted WP2 and WP3 lead to worse air quality in terms of NO_2 and $PM_{2.5}$ from December to February. For PM_{10}, WPs associated with high pollution are roughly evenly distributed throughout the season.

The analysis of interannual variability of the seven regimes through their seasonal frequencies revealed important aspects for interannual predictability of pollution events. The most important mode of climate variability in the tropics and extratropics at interannual timescales, ENSO, was significantly correlated with both polluted and clean WPs. Polluted (clean) patterns were negatively (positively) correlated with ENSO, meaning that La–Niña (El–Niño) years are likely to favor the occurrence of WPs associated with more (less) pollution episodes during the dry season. The fact that ENSO events are related with the frequency of pollution-related weather patterns is a source of predictability of the frequency of high pollution episodes. This provides insight for medium-range air quality forecast for the dry season, and can be a suitable tool to advice decision makers months in advance.

Although we have identified some potential sources of predictability for pollution in Mexico City on the synoptic, intraseasonal, and interannual timescales, work is still needed to evaluate the predictive ability of general circulation models in representing those synoptic patterns. One approach would be to use retrospective forecasts, which could improve synoptic-to-seasonal prediction of air quality in Mexico City.

CRediT authorship contribution statement

Yanet Díaz-Esteban: Conceptualization, Formal analysis, produced the figures, Writing – original draft. **Bradford S. Barrett:** Conceptualization, Writing – original draft. **Graciela B. Raga:** Conceptualization, Writing – original draft.

Declaration of competing interest

The authors declare that they have no known competing financial interests or personal relationships that could have appeared to influence the work reported in this paper.

Acknowledgment

We acknowledge the availability of the public data sets of the European Centre for Medium-Range Weather Forecasts (ERA5), which was highly helpful for this work. Also, the freely available dataset from the Mexican government network, RAMA, was essential to this research. We thank the Secretaría de Medio Ambiente of Mexico City for providing the data of temperature inversions and the Physical Sciences Laboratory of NOAA for the availability of climate indices at the website: https://psl.noaa.gov/data/climateindices/list/.

Appendix A. Supplementary data

Supplementary data to this article can be found online at https://doi.org/10.1016/j.atmosenv.2022.118976.

References

Baklanov, A., Molina, L.T., Gauss, M., 2016. Megacities, air quality and climate. Atmos. Environ. 126, 235–249.
Barrett, B.S., Raga, G.B., 2016. Variability of winter and summer surface ozone in Mexico City on the intraseasonal timescale. Atmos. Chem. Phys. 15, 15359–15370.
Barrett, B.S., Raga, G.B., Retama, A., Leonard, C., 2019. A multiscale Analysis of the tropospheric and stratospheric mechanisms leading to the March 2016 extreme surface ozone event in Mexico city. J. Geophys. Res. Atmos. 124.
Bei, N., Li, G., Zavala, M., Barrera, H., Torres, R., Grutter, M., Gutiérrez, W., García, M., Ruiz-Suarez, L., Ortinez, Y., Gutierrez, A., Alvarado, A., Florez, I., Molina, L.T., 2013. Meteorological overview and plume transport patterns during CalMex 2010. Atmos. Environ. 70, 477–489.
Bravo Cabrera, J.L., Azpra Romero, E., Rodriguez Gonzalez, F.J., Rodriguez López, O., 2018. Effects of ENSO on precipittation in Mexico city. Invest. Geográficas 97 (digital), 2448–7279.
Bravo-Cabrera, J.L., Azpra-Romero, E., Zarraluqui-Such, V., Gay-García, C., 2017. Effects of El Niño in Mexico during rainy and dry seasons: an extended treatment. Atmósfera 30 (3), 221–232.
Burgos-Cuevas, A., Adams, D.K., García-Franco, J.L., Ruiz-Angulo, A., 2021. Seasonal climatology of the Mexico city atmospheric boundary layer. Boundary-Layer Meteorol. 180, 131–154.
Chow, J.C., Watson, J.G., Edgerton, S.A., Vega, E., 2002. Chemical composition of PM2.5 and PM10 in Mexico City during winter 1997. Sci. Total Environ. 287 (3), 177–201.
Chuang, M.-T., Chiang, P.-C., Chan, C.-C., Wang, C.-F., Chang, E.-E., Lee, C.-T., 2008. The effects of synoptical weather pattern and complex terrain on the formation of aerosol events in the Greater Taipei area. Sci. Total Environ. 399, 128–146.
Comrie, A.C., 1996. An all-season synoptic climatology of air pollution in the U.S.-Mexico border region. Prof. Geogr. 48 (3), 237–251.
Curtis, S., Gamble, D., 2008. Regional variations of the Caribbean mid-summer drought. Theor. Appl. Climatol. 94 (1), 25–34.
Davies, D.L., Bouldin, D.W., 1979. A cluster separation measure. IEEE Trans. Pattern. Anal. Mach. Intell. PAMI 1 (2), 224–227.
de Foy, B., Caetano, E., Magaña, V., Zitácuaro, A., Cárdenas, B., Retama, A., Ramos, R., Molina, L., Molina, M., 2005. Mexico City basin wind circulation during the MCMA-2003 field campaign. Atmos. Chem. Phys. 5, 2267–2288.
de Foy, B., Clappier, A., Molina, L., Molina, M.J., 2006a. Distinct wind convergence patterns in the Mexico City basin due to the interaction of the gap winds with the synoptic flow. Atmos. Chem. Phys. 6 (5), 1249–1265. Hal-00295883.
de Foy, B., Fast, J.D., Paech, S.J., Phillips, D., Walters, J.T., Coulter, R.L., Martin, T.J., Pekour, M.S., Shaw, W.J., Kastendeuch, P.P., Marley, N.A., Retama, A., Molina, L.T., 2008. Basin-scale wind transport during the MILAGRO field campaign and comparison to climatology using cluster analysis. Atmos. Chem. Phys. 8, 1209–1224.
de Foy, B., Varela, J.R., Molina, L.T., Molina, M.J., 2006b. Rapid ventilation of the Mexico City basin and regional fate of the urban plume. Atmos. Chem. Phys. 6, 2321–2335.
Donateo, A., Contini, D., Belosi, F., Gambaro, A., Santachiara, G., Cesari, D., Prodi, F., 2012. Characterisation of PM2.5 concentrations and turbulent fluxes on a island of the Venice lagoon using high temporal resolution measurements. Meteorol. Z. 21 (4), 385–398.
Díaz-Esteban, Y., Raga, G.B., 2018. Weather regimes associated with summer rainfall variability over southern Mexico. Int. J. Climatol. 38, 169–186.
Eder, B.K., Davis, J.M., Bloomfield, P., 1994. An automated classification scheme designed to better elucidate the dependence of ozone on meteorology. J. Appl. Meteorol. Climatol. 33 (10), 1182–1199.
Elghazel, H., Benabdeslem, K., 2014. Different aspects of clustering the self-organizing maps. Neural Process. Lett. 39, 97–114.
Fast, J.D., Zhong, S., 1998. Meteorological factors associated with inhomogeneous ozone concentrations within the Mexico City basin. J. Geophys. Res. 103 (D15), 18927–18946.
García-Franco, J.L., 2020. Air quality in Mexico city during the fuel shortage of January 2019. Atmos. Environ. 222, 117131.
Gonçalves, M.L., Netto, M.L.A., Costa, J.A.F., Zullo Júnior, J., 2008. An unsupervised method of classifying remotely sensed images using Kohonen self-organizing maps and agglomerative hierarchical clustering methods. Int. J. Rem. Sens. 29 (11), 3171–3207.
Govender, P., Sivakumar, V., 2020. Application of k-means and hierarchical clustering techniques for analysis of air pollution: a review (1980–2019). Atmos. Pollut. Res. 11, 40–56.
Henderson, G.R., Barrett, B.S., South, K.L., 2017. Eurasian October snow water equivalent: using self-organizing maps to characterize variability and identify relationships to the MJO. Int. J. Climatol. 37, 596–606.
Hersbach, H., Bell, B., Berrisford, P., Biavati, G., Horányi, A., Muñoz-Sabater, J., Nicolas, J., Peubey, C., Radu, R., Rozum, I., Schepers, D., Simmons, A., Soci, C., Dee, D., Thépaut, J.-N., 2018. Era5 hourly data on pressure levels from 1979 to present. Tech. Rep., Copernicus climate change cervices (c3s) climate data store (cds) 10.
Holgate, S.T., 2017. Every breath we take: the lifelong impact of air pollution" – a call for action. Clin. Med. 17 (1), 8–12.
Hsu, C.-H., Cheng, F.-Y., 2016. Classification of weather patterns to study the influence of meteorological characteristics on PM2.5 concentrations in Yunlin County, Taiwan. Atmos. Environ. 144, 397–408.
Hsu, C.-H., Cheng, F.-Y., 2019. Synoptic weather patterns and associated air pollution in Taiwan. Aerosol Air Qual. Res. 19, 1139–1151.
Jain, A.K., Murty, M.N., Flynn, P.J., 1999. Data clustering: a review. ACM Comput. Surv. 31 (3), 264–323.
Jauregui, E., 1988. Local wind and air pollution interaction in the Mexico basin. Atmósfera 1, 131–140.
Jazcilevich, A.D., García, A.R., Caetano, E., 2005. Locally induced surface air confluence by complex terrain and its effects on air pollution in the valley of Mexico. Atmos. Environ. 39, 5481–5489.
Kohonen, T., 1982. Self-organized formation of Topologically correct feature maps. Biol. Cybern. 43 (1), 59–69.
Kohonen, T., 2001. Self-Organizing Maps, third ed. Springer-Verlag, New York.
Kotsakis, A., Choi, Y., Souri, A., Jeon, W., Flynn, J., 2019. Characterization of regional wind patterns using self-organizing maps: impact on dallas–Fort Worth long-term ozone trends. J. Appl. Meteorol. Climatol. 58, 757–772.
Lenschow, P., Abraham, H.-J., Kutzner, K., Lutz, M., Preuß, J.-D., Reichenbächer, W., 2001. Some ideas about the sources of PM10. Atmos. Environ. 35, S23–S33.
Liu, N., Zhou, S., Liu, C., Guo, J., 2019. Synoptic circulation pattern and boundary layer structure associated with PM2.5 during wintertime haze pollution episodes in Shanghai. Atmos. Res. 228, 186–195.
Liu, Y., Weisberg, R.H., 2011. *Self Organizing Maps - Applications And Novel Algorithm Design*, Hard Cover, 702 Pages A Review of Self-Organizing Map Applications in Meteorology and Oceanography. InTech, ISBN 978-953-307-546-4.
Magaña, V., Quintanar, A., 1997. On the use of a general circulation model to study regional climate. In: García, F., Cisneros, G., Fernández-Eguiarte, A., Álvarez, R. (Eds.), Numerical Simulations in the Environmental and Earth Sciences. Cambridge University Press, pp. 39–48.
Magaña, V.O., Vázquez, J.L., Pérez, J.L., Pérez, J.B., 2003. Impact of El Niño on precipitation in Mexico. Geofisc. Int. 42 (3), 313–330.
McGregor, G., Bamzelis, D., 1995. Synoptic typing and its application to the investigation of weather air pollution relationships, Birmingham, United Kingdom. Theor. Appl. Climatol. 51, 223–236.
Morton-Bermea, O., Hernández-Alvarez, E., Almorín-Ávila, M.A., Ordoñezz-Godínez, S., Bermendi-Orosco, L., Retama, A., 2021. Historical trends of metals concentration in PM10 collected in the Mexico City metropolitan area between 2004 and 2014. Environ. Geochem. Health 43, 2781–2798.
Ngang, F., Byun, D., 2011. Classification of weather patterns and associated Trajectories of high-ozone episodes in the Houston–Galveston–Brazoria area during the 2005/06 TexAQS-II. J. Appl. Meteorol. Climatol. 50, 485–499.
Pearce, J.L., Beringer, J., Nicholls, N., Hyndman, R.J., Uotila, P., Tapper, N.J., 2011. Investigating the influence of synoptic-scale meteorology on air quality using self-organizing maps and generalized additive modelling. Atmos. Environ. 45 (1), 128–136.
Perdigón-Morales, J., Romero-Centeno, R., Ordóñez, P., Barrett, B.S., 2018. The midsummer drought in Mexico: perspectives on duration and intensity from the CHIRPS precipitation database. Int. J. Climatol. 38, 2174–2186.
Pozo, D., Marín, J.C., Raga, G.B., Arévalo, J., Baumgardner, D., Córdova, A.M., Mora, J., 2019. Synoptic and local circulations associated with events of high particulate pollution in Valparaiso, Chile. Atmos. Environ. 196, 164–178.
Raga, G., Baumgardner, D., Kok, G., Rosas, I., 1999. Some aspects of boundary layer evolution in Mexico City. Atmos. Environ. 33 (30), 5013–5021.
Retama, A., D, B., Raga, G.B., McMeeking, G.R., Walker, J.W., 2015. Seasonal and diurnal trends in black carbon properties and co-pollutants in Mexico City. Atmos. Chem. Phys. 15, 9693–9709.

Reynolds, R.W., Rayner, N.A., Smith, T.M., Stokes, D.C., Wang, W., 2002. An improved in situ and satellite SST analysis for climate. J. Clim. 15, 1609–1625.
Rodríguez-Vera, G., Romero-Centeno, R., Castro, C.L., Castro, V.M., 2019. Coupled interannual variability of wind and sea surface temperature in the Caribbean sea and the Gulf of Mexico. J. Clim. 32, 4263–4280.
Romero-Centeno, R., Zavala-Hidalgo, J., Raga, G.B., 2007. Midsummer gap winds and low-level circulation over the eastern tropical Pacific. J. Clim. 20, 3768–3784.
Salcido, A., Carreón-Sierra, S., Celada Murillo, A.T., 2019. Air pollution flow patterns in the Mexico city region. Climate 7, 128.
Salvador, P., Artíñano, B., Alonso, D.G., Querol, X., Alastuey, A., 2004. Identification and characterisation of sources of PM10 in Madrid (Spain) by statistical methods. Atmos. Environ. 38 (3), 435–447.
Sheppard, P.R., Comrie, A.C., Packin, G.D., Angersbach, K., Hughes, M.K., 2002. The climate of the US Southwest. Clim. Res. 21, 219–238.
Sheridan, S.C., Lee, C.C., 2011. The Self-Organizing Map in synoptic climatological research. Prog. Phys. Geogr. 35 (1), 109–119.
Silva-Quiroz, R., Rivera, A.L., Ordoñez, P., Gay-García, C., Frank, A., 2019. Atmospheric blockages as trigger of environmental contingencies in Mexico City. Heliyon 5, e02099.
Stauffer, R.M., Thompson, A.M., Young, G.S., 2016. Tropospheric ozonesonde profiles at long-term U.S. monitoring sites: 1. A climatology based on self-organizing maps. J. Geophys. Res. Atmos. 121 (3), 1320–1339.
Vega, E., Reyes, E., Sánchez, G., Ortiz, E., Ruiz, M., Chow, J., Watson, J., Edgerton, S., 2002. Basic statistics of PM2.5 and PM10 in the atmosphere of Mexico City. Sci. Total Environ. 287 (3), 167–176.
Velasco, E., Retama, A., 2017. Ozone's threat hits back Mexico city. Sustain. Cities Soc. 31, 260–263.
Vesanto, J., Alhoniemi, E., 2000. Clustering of the self-organizing map. IEEE Trans. Neural Network. 11, 586–600.
World Health Organization, 2018. Ambient (Outdoor) Air Pollution. URL. https://www.who.int/en/news-room/fact-sheets/detail/ambient-(outdoor)-air-quality-and-health.
Zhan, C.-c., Xie, M., Fang, D.-x., Wang, T.-j., Wu, Z., Lu, H., Li, M.-m., Chen, P.-l., Zhuang, B.-l., Li, S., Zhang, Z.-q., Gao, D., Ren, J.-y., Zhao, M., 2019. Synoptic weather patterns and their impacts on regional particle pollution in the city cluster of the Sichuan Basin, China. Atmos. Environ. 208, 34–37.